


# Noninvasive pulmonary artery pressure monitoring by EIT: a model-based feasibility study

Martin Proença<sup>1,2</sup>  · Fabian Braun<sup>1,2</sup> · Josep Solà<sup>1</sup> · Jean-Philippe Thiran<sup>2,3</sup> · Mathieu Lemay<sup>1</sup>

Received: 28 March 2016 / Accepted: 7 September 2016 / Published online: 17 September 2016  
© International Federation for Medical and Biological Engineering 2016

**Abstract** Current monitoring modalities for patients with pulmonary hypertension (PH) are limited to invasive solutions. A novel approach for the noninvasive and unsupervised monitoring of pulmonary artery pressure (PAP) in patients with PH was proposed and investigated. The approach was based on the use of electrical impedance tomography (EIT), a noninvasive and safe monitoring technique, and was tested through simulations on a realistic 4D bio-impedance model of the human thorax. Changes in PAP were induced in the model by simulating multiple types of hypertensive conditions. A timing parameter physiologically linked to the PAP via the so-called pulse wave velocity principle was automatically estimated from the EIT data. It was found that changes in PAP could indeed be reliably monitored by EIT, irrespective of the pathophysiological condition that caused them. If confirmed clinically, these findings could open the way for a new generation of noninvasive PAP monitoring solutions for the follow-up of patients with PH.

**Keywords** Noninvasive pulmonary artery pressure (PAP) · Pulmonary hypertension · Electrical impedance tomography (EIT) · Pulse wave velocity (PWV) · 4D bio-impedance model

## 1 Introduction

Pulmonary hypertension (PH) is a pathophysiological condition defined as an increase in mean pulmonary artery pressure (PAP) above 25 mmHg at rest as assessed by right heart catheterization [12]. In an observational study, the prevalence of PH in an unselected population was found to be of at least 326 cases/100,000 [57]. Untreated or inadequately treated PH is fatal as it ultimately leads to right ventricular heart failure [12].

After initiation of PH therapy, the follow-up of the patient's health status is often limited to punctual invasive measurements at the clinic at intervals of months [12, 33], which makes the anticipation of worsening conditions complex between clinic visits. In perioperative settings, PH is a major cause of risks and complications [13]. The benefits and safety of invasive procedures (pulmonary artery catheterization) have raised serious concerns due to the lack of evidence showing any decrease in morbidity and mortality following their use [16]. The need for a safer solution for the clinical management of patients with PH is thus strong. An optimal PAP monitoring modality should be noninvasive (free of any risks or complications, and thus compatible with frequent measurements) and unsupervised (able to operate without supervision of a medical doctor) [1]. Such a modality does not currently exist.

In the present study, we propose and investigate the potential of a novel noninvasive, continuous and unsupervised PAP monitoring approach based on the pulse wave velocity (PWV) principle and the use of electrical impedance tomography (EIT).

### 1.1 The pulse wave velocity principle

The PWV is the velocity at which a pressure wave travels along the wall of an artery by expanding it. The PWV

✉ Martin Proença  
map@csem.ch

<sup>1</sup> Centre Suisse d'Electronique et de Microtechnique (CSEM), Neuchâtel, Switzerland

<sup>2</sup> Ecole Polytechnique Fédérale de Lausanne (EPFL), Lausanne, Switzerland

<sup>3</sup> University Hospital Center (CHUV) and University of Lausanne (UNIL), Lausanne, Switzerland

principle states that this velocity will be higher if said artery is stiffer [62]. It follows that PWV and blood pressure are intrinsically linked as arterial stiffness induces rises in both PWV and blood pressure [62]:

$$\text{Arterial Stiffness} \nearrow \Rightarrow \begin{array}{l} \text{Blood Pressure} \nearrow \\ \text{Pulse Wave Velocity} \nearrow \end{array}$$

The arrows simply indicate how each parameter relates to the others, but do not necessarily imply linearity (the relationship between blood pressure and PWV is typically nonlinear [37]). This physiological principle is the basis of numerous noninvasive systemic blood pressure monitoring devices, as PWV can easily be measured noninvasively in the systemic circulation from superficial arteries [54]. However, as the pulmonary circulation has no superficial arteries, the noninvasive monitoring of the PWV in the lungs—and therefore the noninvasive monitoring of the PAP via the PWV principle—remains a challenge.

## 1.2 Noninvasive monitoring of the pulmonary PWV

EIT is a safe, low-cost and noninvasive monitoring technique that reconstructs the likely distribution of intrathoracic impedance from measurements performed with a belt of electrodes attached around the thorax [20]. In the lungs, impedance is predominantly affected by respiratory activity: Cardiovascular-related impedance changes, associated with the pulsatility of the pulmonary arteries, are of much smaller amplitude [11]. The functional analysis of these pulsatile changes in pulmonary impedance is hypothesized to allow extracting parameters related to the pulmonary PWV, and thus information about the underlying PAP [56]. This is precisely the approach targeted in the present study, as further detailed hereafter.

Let us consider the ejection of blood by the right ventricle starting with the opening of the pulmonary valve at time  $t = 0$ . The resulting pressure pulse propagates at a certain velocity (the PWV) to the various branches of the pulmonary arterial tree. At any downstream arterial site  $\mathbf{x}$ , the passage of the pressure pulse distends the arterial wall (Fig. 1a) with a pressure  $p(\mathbf{x}, t)$  (Fig. 1b). The local distension of the arterial wall induced by  $p(\mathbf{x}, t)$  induces a local variation in electrical conductivity  $\sigma(\mathbf{x}, t)$  (Fig. 1c). Consequently,  $p(\mathbf{x}, t)$  and  $\sigma(\mathbf{x}, t)$  are inherently synchronous, as the former induces the latter. Therefore,  $p(\mathbf{x}, t)$  and  $\sigma(\mathbf{x}, t)$  are expected to have identical pulse transit times (PTT), i.e., the time required by the pressure pulse to reach location  $\mathbf{x}$  in the arterial tree (see dashed line in Fig. 1b, c). The PTT being, by definition, inversely proportional to the PWV, we hypothesize that tracking changes in pulmonary PWV, and therefore in PAP (PWV principle), can be done by tracking changes in the PTT of  $\sigma(\mathbf{x}, t)$  assessed by EIT:

$$\text{PAP} \nearrow \iff \text{PWV} \nearrow \iff \text{EIT-derived PTT} \searrow$$

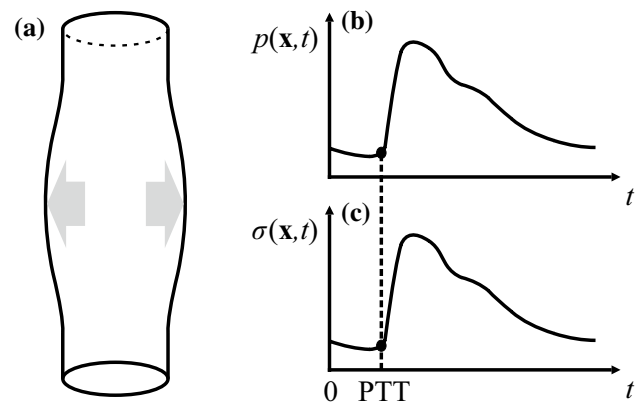


**Fig. 1** **a** At each cardiac cycle, the wall of the artery is distended by the passage of a pressure pulse. **b** The pressure exerted by blood at a given location  $\mathbf{x}$  along the wall is described by  $p(\mathbf{x}, t)$ . **c** The small change in blood volume induced by this distension creates a small increase in electrical conductivity  $\sigma(\mathbf{x}, t)$ . Both waveforms ( $p(\mathbf{x}, t)$  and  $\sigma(\mathbf{x}, t)$ ) being inherently synchronous, their timing information—namely their PTT—is identical

## 1.3 Previous work and study goal

The use of EIT for monitoring patients with PH has previously been proposed by the group of Smit et al. [53]. They observed a decreased maximal pulmonary systolic impedance change ( $\Delta Z_{\text{sys}}$ ) in patients suffering from advanced stages of idiopathic pulmonary arterial hypertension.  $\Delta Z_{\text{sys}}$  was hypothesized to represent pulmonary perfusion and its decrease to originate mostly from the reduction of the vascular bed. However, the physiological link between the amplitude information of the pulmonary impedance change and the PAP remains to this day unclear, as  $\Delta Z_{\text{sys}}$  may not unequivocally be representative of perfusion [5, 18]. Conversely, the timing information of the pulmonary impedance change has a direct physiological link to the PAP through the PWV principle.

We have previously demonstrated the feasibility of this PWV-based approach experimentally for blood pressure monitoring in the systemic circulation [55]. In the present study, we investigate its feasibility for the pulmonary circulation using simulations on a 4D bio-impedance model of the human thorax.

## 2 Methods

We test our approach on a model as this offers several advantages over clinical data: (1) We can easily simulate various PAP-affecting pathological conditions, in particular different types of PH, thus avoiding protocol- or pathology-specific results that could arise from clinical data; (2) we can freely induce PAP variations, be they small or large;

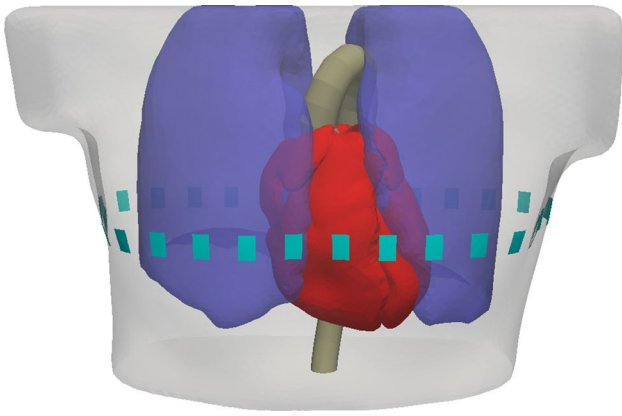


**Fig. 2** 4D thoracic bio-impedance model developed by our group [6], shown here at end diastole ( $t = 0$ ). The model includes MRI-based 4D bio-impedance models of the heart and the aorta, and a simplified 4D bio-impedance model of the pulmonary vasculature. Each mesh element is at a fixed location, and its conductivity  $\sigma(\mathbf{x}, t)$  varies over the time course of the cardiac cycle, in function of the organ or anatomical structure occupying the location of the element at time  $t$ . The small rectangles on the periphery of the thorax depict the EIT electrodes

(3) we do not depend on reference hemodynamic variables measured in clinical settings, which can be difficult to obtain (e.g., pulmonary PWV) or affected by transient hemodynamics (e.g., PAP) [46].

## 2.1 Thoracic bio-impedance model

### 2.1.1 Main components and functionalities

The 4D thoracic bio-impedance model aims at simulating the changes in conductivity occurring inside the thorax over the course of a cardiac cycle. Only conductivity changes associated with cardiac activity are modeled; respiration-related changes are not included (the validity of this simplification is discussed in Sect. 4).

We use a modified version of the 4D bio-impedance model developed by our group [6]. This model, shown in Fig. 2, consists in a mesh of a human thorax where each mesh element is at a fixed location  $\mathbf{x}$  and has a conductivity value  $\sigma(\mathbf{x}, t)$  that varies over time, in function of the organ or anatomical structure occupying the location of the element at time  $t$ . The model describes cardiac-related conductivity changes induced by the heart, the aorta and the lungs. The geometrical deformations of the cardiac chambers and the aorta are directly based on 4D magnetic resonance imaging (MRI) scans of a healthy male volunteer (62 kg, 178 cm, 28 years old). The same could obviously not be done for the pulmonary arterial tree, due to the size of its microvasculature and the limited resolution of MRI scans, which is why a simplified model of the pulmonary

vasculature was implemented in [6]. In the present study, we replace this pulmonary model by a 4D bio-impedance model of a realistic pulmonary arterial tree.

To build this pulmonary model, we start by building an anatomically realistic static 3D model of the whole pulmonary arterial tree (Sect. 2.1.2). Then, in order to dynamize it (i.e., to make it 4D by simulating the pressure-induced distension of its arteries over time), we use a hemodynamic model of the pulmonary circulation (Sect. 2.1.3). Finally, we transform this 4D model into a 4D bio-impedance model by describing how the pressure-induced distension of the pulmonary arteries affects the conductivity  $\sigma(\mathbf{x}, t)$  in the lungs (Sect. 2.1.4).

### 2.1.2 Anatomical model of the pulmonary arterial tree

The creation of the 3D anatomical model of the pulmonary arterial tree was a two-step process. As a first step, an anatomically accurate model of the large pulmonary arteries by Reymond [45]—based on contrast-enhanced magnetic resonance angiography scans—was rigidly registered onto our corresponding MRI-based arteries.

As a second step, the remaining (medium and small) arteries were generated using a validated shape-dependent volume-filling branching algorithm [7]: The lung volumes were automatically filled with a branching tree using the end segments of the large arteries as seed points for the tree growing procedure. The resulting 3D pulmonary arterial tree is shown in Fig. 3. The tree growing procedure was controlled through appropriate branching and asymmetry ratios [40] and stopped when the smallest vessels reached a radius of 0.01 mm (pre-capillary vessels) [21]. Therefore, the obtained model accurately describes the geometry and morphometry of a realistic pulmonary arterial tree.

### 2.1.3 Circulatory model of the pulmonary arterial tree

Several circulatory models exist to assess the distribution of pressure and flow in the pulmonary arterial tree [44, 45, 63]. Some models, such as the 1D distributed parameter model validated by Reymond [45], focus on the larger segments of the arterial tree, where nonlinear effects occur and numerical solving schemes are required. Solving such models numerically for the entire tree is computationally infeasible, which is why linearized models are typically used for the smaller arteries and provide analytical solutions for pressure and flow [40]. In the present study, Reymond's 1D distributed parameter model will be used to assess the distribution of pressure and flow in the larger arteries of the pulmonary arterial tree whereas a linearized solution will be used for the smaller arteries, where nonlinear effects are negligible. Hereafter, we therefore briefly present 1D distributed parameter models, such as Reymond's model. We

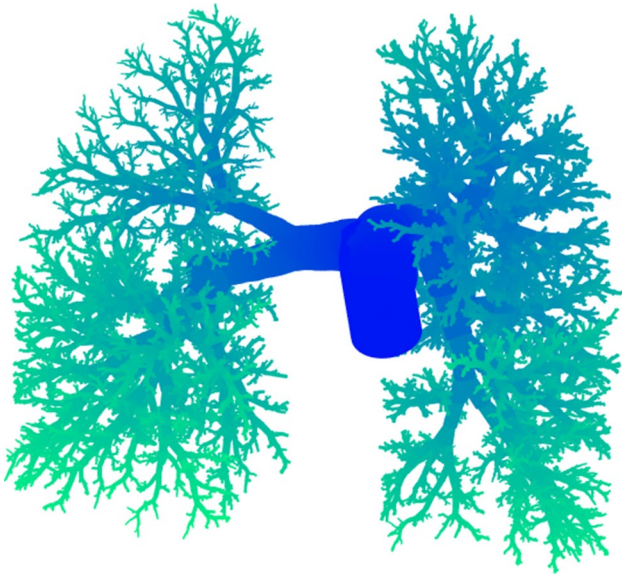


**Fig. 3** Anatomical model of the pulmonary arterial tree. To help the visualization, not all smaller arteries are shown and a color code is used to illustrate the distance from the pulmonary valve (dark blue = close; light green = far)

then explain how the governing equations of 1D distributed parameter models can be linearized for the small arteries and how analytical solutions can be derived. Finally, we detail the inflow and outflow boundary conditions we used for both Reymond's model for the large arteries and the linearized model for the small arteries.

**Circulatory model for the large arteries** In a 1D distributed parameter model, arteries are considered as long straight tapering segments of length  $l$  and time- and location-dependent cross-sectional area  $A(x, t)$  [59] (see Fig. 4). The blood running through the artery is subjected to a pressure  $p(x, t)$  and flows at a rate  $q(x, t)$ . Both quantities are assessed by solving the integral form of the continuity and longitudinal momentum Navier–Stokes equations [40, 45]. The system of equations consists of three unknowns, namely pressure ( $p$ ), flow ( $q$ ) and arterial cross-sectional area ( $A$ ). An empirically derived state equation describing the viscoelastic properties of the arterial wall is used to complete the system [4, 45]. The three-unknown system is then solved numerically, as no analytical solution exists. In the present study, we use Reymond's 1D distributed parameter model [45] developed for the systemic circulation and adapted by Billiet [4] for the pulmonary circulation. A more detailed description of 1D distributed parameter models can be found in [40] and [59].

**Circulatory model for the small arteries** For the small arteries, the complexity required for solving the aforementioned three-unknown system becomes computationally infeasible due to the size of the pulmonary tree [40].

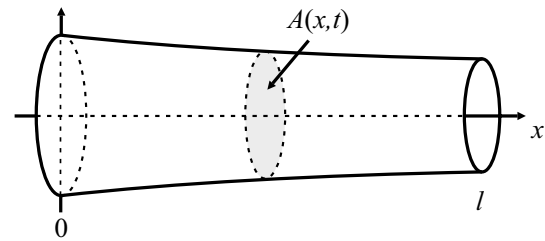


**Fig. 4** Model of a large arterial segment (tapering tube) of length  $l$  and cross-sectional area  $A(x, t)$

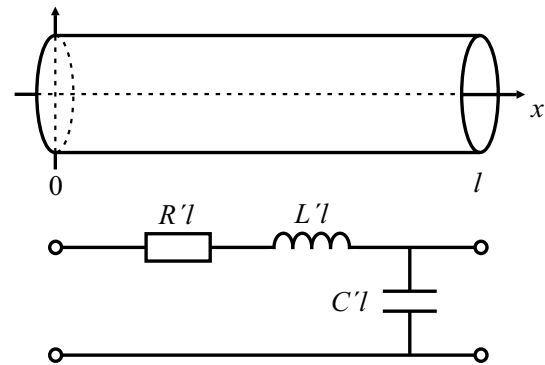


**Fig. 5** Upper panel Model of a small arterial segment (non-tapering tube) of length  $l$ . Lower panel Electrical analog, with  $R'$ ,  $L'$  and  $C'$  the electrical resistance, inductance and capacitance per unit length, respectively, mimicking their hydraulic counterparts

However, as smaller arteries do not taper significantly, the convective acceleration term in the longitudinal momentum Navier–Stokes equation becomes negligible [9, 52] and the state equation can be simplified [40]. The linearization of the governing equations becomes possible [40], and an analytical solution for pressure and flow can be found in every arterial segment of the tree [63]. These solutions make heavy use of transmission line theory (by analogy with electrical circuits), as small (non-tapering) arterial segments can be modeled by electrical analogs (Fig. 5). We implemented these analytical solutions for pressure and flow in the small arteries following the approach proposed by Wiener et al. [63]. A more detailed description of linearized circulatory models for small arteries can be found in [40].

**Boundary conditions** Solving Reymond's nonlinear model for the large arteries and the linearized model for the small arteries requires the definition of inflow and outflow boundary conditions. To do so, it is first essential to define the arterial sites in the tree where the transition between the large and the small arteries occurs, i.e., the sites where the transition between the nonlinear and the linearized model will take place. Let us call them transition sites.

From a hemodynamic viewpoint, large arteries are dominated by inertial effects whereas small arteries are

dominated by viscous effects [62]. As a ratio of inertial over viscous forces, the so-called Womersley number  $\alpha$  is therefore a well-suited criterion for classifying arteries as either large (dominated by inertial effects: large  $\alpha$ ) or small (dominated by viscous effects: small  $\alpha$ ) [62]. Milnor [34] measured Womersley numbers at multiple arterial sites and found that large elastic arteries typically show Womersley numbers  $\alpha \geq 4$ . Therefore, we can define our transition sites as the last arterial segments in the tree (starting from the heart) for which  $\alpha \geq 4$ .

Let us now introduce the inflow and outflow boundary conditions for the large arteries. A typical inflow boundary condition in 1D distributed parameter models such as Reymond’s is a flow waveform [40]. We use the waveform proposed by [39], as it can easily be scaled to any desired cardiac output (CO) and heart rate:

$$q(0, t) = \frac{CO \cdot t}{\tau_p^2} \exp\left(-\frac{t^2}{2\tau_p^2}\right), \tag{1}$$

with  $t \in [0, T[$ , where  $T$  is the cardiac period and  $\tau_p$  is the time to peak flow (acceleration time). This time is inversely related to the PAP and can be empirically derived from it as [23]:

$$\tau_p = \frac{1}{6.8} [2.1 - \log_{10}(P_A)], \tag{2}$$

where  $P_A$  is the mean PAP.

As outflow boundary condition, Reymond’s model uses three-element Windkessel models at all transition sites [45]. These models are frequently used to mimic the afterload of the heart [61]. In Reymond’s model, they are used to mimic the equivalent impedance of the tree branches “seen” from each transition site downstream. These equivalent impedances are known in our study from the 3D anatomical model of the pulmonary arterial tree. With both its inflow and outflow conditions defined, Reymond’s model can now be solved.

Solving Reymond’s model provides us directly with the inflow boundary conditions for the small arteries, as it determines the flow waveforms entering each transition site, i.e., entering the small arteries. On the other hand, the outflow boundary conditions for the small arteries in linearized circulatory models are typically set by controlling the value of the pressure downstream of the arterial tree [40] (let us call it  $P_W$ , see Fig. 6). Formally speaking,  $P_W$  represents the pressure of the capillaries or the venous microvasculature, which is difficult to measure in clinical practice. It is, however, essentially the same as pulmonary capillary wedge pressure if we neglect the small transvenous pressure gradient [32], and is assumed to be continuous; we discuss the validity of this assumption in Sect. 4.

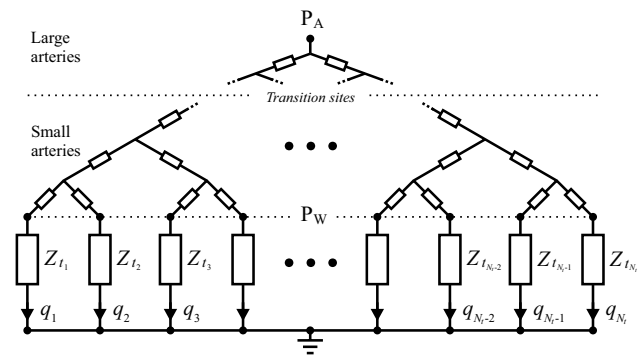


**Fig. 6** Schematic representation of the pulmonary arterial tree, by analogy with electrical circuits. The tree is made of large and small arteries. In the large arteries, nonlinear effects are non-negligible and the distribution of pressure and flow in the arterial network requires a numerical solution. From the so-called transition sites and beyond, the distribution of pressure and flow in the arterial network can be solved analytically after linearization of the problem. Each terminal arterial segment in the tree (pre-capillary artery) is connected to a terminal impedance  $Z_{t_i}$  that allows controlling the value of the pressure  $P_W$  at the output of the tree

Setting  $P_W$  to a given desired value in structured tree models is typically done through the use of  $N_t$  terminal impedances  $Z_{t_i}$  ( $i \in \{1, \dots, N_t\}$ ) at the leaves of the tree [40] (Fig. 6). The value of each terminal impedance  $Z_{t_i}$  must be properly set in order to ensure its upstream pressure to equal  $P_W$ . This requires finding the flow  $q_i$  running through each  $i$ -th leaf of the tree, as  $Z_{t_i} = P_W/q_i, \forall i \in \{1, \dots, N_t\}$ . These flow values can easily be obtained by momentarily setting  $Z_{t_i} = 0$  for all terminal impedances and imposing the desired transarterial pressure gradient ( $P_A - P_W$ ) at the input of the tree.

#### 2.1.4 Assessment of pulmonary conductivity

Transforming our 4D model into a 4D bio-impedance model requires assessing the effective conductivity of lung parenchyma  $\sigma(\mathbf{x}, t)$  at every location  $\mathbf{x}$  in the lungs. During breath hold,  $\sigma(\mathbf{x}, t)$  is predominantly affected by arterial pulsatility. The distension of the arterial bed makes the conductivity of lung parenchyma slightly rise above its end-diastolic value  $\sigma(\mathbf{x}, 0)$  during systole (i.e., for  $t > 0$ ), due to the high conductivity of blood ( $\sigma_{blood} \approx 0.7$  S/m at EIT frequencies) [17]. This end-diastolic value of lung parenchyma  $\sigma(\mathbf{x}, 0)$  is difficult to estimate as it depends on the conductivity of lung alveolar tissue  $\sigma_{alv}$ , which depends on the fractional volume of air in the lungs. Several mathematical models have been developed to express  $\sigma_{alv}$  as a function of the degree of deflation of the lungs. Roth et al. [47] compared several of these models and introduced their own, based on 3D alveolar microstructures. For lung tissue imaged at functional lung capacity as

is the case in our model, their observations suggest an average value  $\sigma_{alv} = 0.1$  S/m [47]. This conductivity value does not include extra-capillary blood vessels, i.e., the arteries and veins. In order to obtain the effective conductivity of the whole lung parenchyma  $\sigma(\mathbf{x}, t)$  (including extra-capillary blood vessels), Nopp et al. [38] suggested to consider lung tissue as a mixture of a dielectric medium (alveolar tissue with conductivity  $\sigma_{alv}$ ) and conductive inclusions (extra-capillary blood vessels with conductivity  $\sigma_{blood}$ ). The Maxwell Garnett mixing rule states that [24]:

$$\sigma(\mathbf{x}, t) = \sigma_m + \frac{\frac{1}{3}f_i(\sigma_i - \sigma_m) \sum_{k=1}^3 \frac{\sigma_m}{\sigma_m + N_k(\sigma_i - \sigma_m)}}{1 - \frac{1}{3}f_i(\sigma_i - \sigma_m) \sum_{k=1}^3 \frac{N_k}{\sigma_m + N_k(\sigma_i - \sigma_m)}}, \quad (3)$$

where  $\sigma_m = \sigma_{alv}$  and  $\sigma_i = \sigma_{blood}$  are the conductivities of the dielectric medium and the inclusions, respectively,  $f_i = f_i(\mathbf{x}, t)$  is the volume fraction of the inclusions,  $N_k$  are the depolarization factors, and  $k \in \{1, 2, 3\}$  corresponds to the three Cartesian coordinates. For cylindrical inclusions such as arterial segments,  $N_{1,2} \approx 0.5$  and  $N_3 \approx 0$  [24]. Via our anatomical model of the pulmonary arterial tree, the volume fraction of blood vessels  $f_i(\mathbf{x}, t)$  can be assessed in each pulmonary voxel  $\mathbf{x}$  over time, with pulmonary venous blood volume approximately equal to the non-pulsatile (end diastolic) component of arterial blood volume [15]. For instance, in a small pulmonary voxel at location  $\mathbf{x}$  whose volume is occupied at 10 % by arteries at end diastole ( $t = 0$ ), the volume fraction of blood will be  $f_i(\mathbf{x}, 0) = 0.2$  (10 % of arterial blood and 10 % of venous blood). The remaining 80 % will be occupied by lung alveolar tissue with conductivity  $\sigma_{alv}$ . Using (3), this gives us  $\sigma(\mathbf{x}, 0) = 0.17$  S/m in that particular pulmonary voxel. As the cardiac cycle unfolds ( $t > 0$ ) and systole occurs, the arteries distend with the increase in pressure. We can precisely determine the extent of this arterial distension thanks to the circulatory model. With this distension, the increase in arterial blood volume and therefore  $f_i(\mathbf{x}, t)$  is known at each instant of the cardiac cycle. As a consequence, via (3), the value of  $\sigma(\mathbf{x}, t)$  is also known for every location  $\mathbf{x}$  in the lungs and for the whole cardiac cycle, which completes the creation of our 4D bio-impedance model.

## 2.2 Simulation of pathologies

The hemodynamic behavior of our 4D thoracic bio-impedance model is controlled by a set of hemodynamic parameters:  $P_A$ ,  $P_W$ ,  $CI$ ,  $R_t$ , and  $C_t$ .

### 2.2.1 Hemodynamic parameters description, interdependencies and normal values

A hemodynamic characteristic of the pulmonary circulation is that the product of the pulmonary vascular resistance  $R_t$

and compliance  $C_t$  is a constant (at a given downstream left atrial pressure) [58]. It is commonly referred to as the pulmonary RC time  $\tau$ . In a retrospective study on large clinical datasets, Tedford et al. [58] derived the following relationship with pulmonary capillary wedge pressure  $P_W$ :

$$\tau = -0.0063 \cdot P_W + 0.46. \quad (4)$$

As a consequence, except for particular conditions affecting left atrial pressure and thus  $P_W$ , the pulmonary RC time  $\tau$  remains constant in health and hypertension [26, 27, 49]. Although  $\tau$  is related to heart rate (HR) [27, 49], any reduction in  $R_t$  and related increase in  $C_t$  during hypertension treatment has been shown not to be due to a change in HR, and therefore the latter is constant in the model (HR = 80 bpm) [27].

In their literature review on pulmonary hemodynamics in normal subjects, Kovacs et al. [25] reported normal values for  $R_t$  of  $0.056 \pm 0.023$  mmHg · s/mL. In our model,  $R_t$  can directly be obtained from the anatomical model of the pulmonary arteries as the equivalent resistance of the entire tree [62]. We obtain  $R_t = 0.048$  mmHg · s/mL, which is well in line with the aforementioned value reported by Kovacs et al. They also reported normal mean PAP ( $P_A = 14.0$  mmHg) and pulmonary capillary wedge pressure ( $P_W = 8.0$  mmHg) values, which yield  $\tau = 0.41$  s via (4). We can then obtain the pulmonary vascular compliance  $C_t$  using the definition of the pulmonary RC time:

$$C_t = \tau/R_t, \quad (5)$$

which gives us  $C_t = 8.478$  mL/mmHg. Lastly, we can find the cardiac index (CI), i.e., the cardiac output (CO) normalized by the body surface area (BSA):

$$CI = \frac{CO}{BSA} = \frac{P_A - P_W}{R_t \cdot BSA}. \quad (6)$$

With  $BSA = 1.78$  m<sup>2</sup> calculated using the Du Bois formula [10], we find  $CI = 4.19$  L/min/m<sup>2</sup>, which is well in line with the value of 4.10 L/min/m<sup>2</sup> reported by Kovacs et al.

The list of normal hemodynamic parameters obtained for the normotensive (non-pathological) vascular state is summarized in the first row of Table 1.

### 2.2.2 Simulation of pulmonary hypertensive conditions

By modifying the hemodynamic parameters controlling the model, several hypertensive conditions can be realistically simulated and allow us to test our approach in various forms of PH.

PH is clinically classified into five groups: pulmonary arterial hypertension, PH due to left heart disease, PH due to lung diseases and/or hypoxia, chronic thromboembolic PH and PH with unclear and/or multifactorial mechanisms [12]. We aim at simulating one

**Table 1** Normal and pathology-specific hemodynamic parameter values of the model

Pathology	$P_A$ (mmHg)	$P_W$ (mmHg)	CI (L/min/m <sup>2</sup> )	$R_t$ (mmHg · s/mL)	$C_t$ (mL/mmHg)
None	14.0	8.0	4.19	0.048	8.478
PAH	24.0	8.0	2.82	0.191	2.141
	34.0	8.0	2.63	0.334	1.225
	44.0	8.0	2.55	0.477	0.858
	54.0	8.0	2.50	0.620	0.660
	64.0	8.0	2.48	0.764	0.536
PH-LHD	24.0	15.3	2.66	0.111	3.284
	34.0	22.6	2.23	0.173	1.835
	44.0	29.9	2.02	0.236	1.154
	54.0	37.2	1.91	0.298	0.758
	64.0	44.5	1.83	0.360	0.499
HAPE	24.0	12.0 <sup>a</sup>	3.70	0.110 <sup>b</sup>	3.107
	34.0	17.0 <sup>a</sup>	3.70	0.155 <sup>b</sup>	1.813
	44.0	22.0 <sup>a</sup>	3.70	0.201 <sup>b</sup>	1.280
	54.0	27.0 <sup>a</sup>	3.70	0.246 <sup>b</sup>	0.989
	64.0	32.0 <sup>a</sup>	3.70	0.292 <sup>b</sup>	0.806
CTEPH	24.0	8.0	2.51	0.215	1.905
	34.0	8.0	2.30	0.382	1.073
	44.0	8.0	2.22	0.549	0.747
	54.0	8.0	2.17	0.715	0.573
	64.0	8.0	2.14	0.882	0.464

*PAH* Pulmonary arterial hypertension, *PH-LHD* pulmonary hypertension due to left heart disease, *HAPE* high-altitude pulmonary edema, *CTEPH* chronic thromboembolic pulmonary hypertension,  $P_A$  mean pulmonary artery pressure,  $P_W$  mean pulmonary capillary wedge pressure, CI cardiac index,  $R_t$  pulmonary vascular resistance,  $C_t$  pulmonary vascular compliance.

<sup>a</sup> These values actually represent capillary pressure  $P_C$ , not pulmonary capillary wedge pressure  $P_W$ . As detailed in Sect. 2.2.2,  $P_W$  in HAPE is actually normal (10.0 mmHg) [31] whereas  $P_C$  is abnormally elevated. Increasing  $P_W$  in the model can simulate either an increase in  $P_W$  (as is the case in PH-LHD) or an increase in transvenous pressure gradient (as is the case in HAPE)

<sup>b</sup> As the values provided for  $P_W$  actually represent  $P_W$  (see previous note), these  $R_t$  values actually represent pulmonary arterial resistance only, not the true values of the entire pulmonary vascular resistance. Those can be obtained using (6) with  $P_W = 10.0$  mmHg for all levels of HAPE [31]

pathological case of each group, except for the last one, since its pathogenesis is unclear. For each pathological case considered, five levels of PAP above the non-pathological value (14 mmHg) will be considered, by increments of 10 mmHg (i.e.  $P_A = \{24, 34, 44, 54, 64\}$  mmHg). The case  $P_A = 24$  mmHg simulates a borderline pre-hypertensive stage, as PH is only formally diagnosed for  $P_A \geq 25$  mmHg [12]. The remaining cases (34 to 64 mmHg) represent mild to severe levels of PAP.

*Pulmonary arterial hypertension (PAH)* PAH is characterized by the vasoconstriction, muscularization and fibrosis of the small pulmonary arteries (< 0.5 mm of diameter) [12]. The loss of distensibility that results from this vascular remodeling process progressively induces an overall decrease in arterial compliance in the whole tree [28, 48]. In our model, we simulate PAH by reducing the diameter of the small arteries—thus increasing  $R_t$ —and  $C_t$

decreases accordingly (via (5)) as the pulmonary RC time ( $\tau$ ) does not change in hypertension [58].

In order to simulate the various levels of PAH, let us first consider the average hemodynamic parameter values in PAH reported by Humbert et al. [22] from a French national registry:  $P_A = 55.0$  mmHg,  $P_W = 8.0$  mmHg (unaffected in PAH) and  $CI = 2.5$  L/min/m<sup>2</sup>. We find the corresponding  $R_t$  value (0.635 mmHg · s/mL) with (6). With the baseline  $P_A$  (14.0 mmHg) and  $R_t$  (0.048 mmHg · s/mL) values found earlier for the normotensive case (Sect. 2.2.1), we now have two  $\{P_A, R_t\}$  pairs, which allows us to predict  $R_t$  as a function of  $P_A$ , as both quantities are linearly related in the pulmonary circulation [49]. We obtain:

$$R_t = 0.0143 \cdot P_A - 0.1519. \tag{7}$$

Finally, we obtain the values of CI for each level of PAP using (6).

The complete list of thus obtained hemodynamic parameter values to simulate each level of PAH is provided in Table 1.

*PH due to left heart disease (PH-LHD)* In the second group of pulmonary PH, the failure of the left heart to pump blood efficiently—as in cases of valvular diseases or advanced stages of heart failure—leads to an elevation of left heart pressures [14]. This rise in  $P_W$  causes an elevation of  $P_A$  upstream, either in a passive ( $P_A - P_W \leq 12$  mmHg) or in a reactive ( $P_A - P_W > 12$  mmHg) manner [12]. In passive PH-LHD,  $R_t$  remains normal while it can significantly increase in cases of reactive PH-LHD due to capillary and arterial remodeling [14]. In a retrospective study in heart failure patients, Afshar et al. [3] reported the following average hemodynamic parameters:  $P_A = 38.0$  mmHg,  $P_W = 25.5$  mmHg and  $CI = 2.13$  L/min/m<sup>2</sup>. From these values and the baseline  $P_A$  and  $P_W$  values found for the normotensive case (Sect. 2.2.1), we can predict  $P_W$  for all levels of PAP as experimental data show a quasi-linear relationship between  $P_A$  and  $P_W$  in PH-LHD [3]:

$$P_W = 0.73 \cdot P_A - 2.21. \quad (8)$$

Proceeding as for PAH, we then find  $R_t$  and  $CI$  for all levels of PAP. A particularity of PH-LHD is that the drastic increase in left atrial pressure significantly decreases the pulmonary RC time  $\tau$  via (4). This diminution of  $\tau$  is principally due to a significant decrease in compliance [58], as  $R_t$  remains either unchanged (passive PH-LHD) or is markedly augmented (active PH-LHD).

The complete list of thus obtained hemodynamic parameter values to simulate each level of PH-LHD is provided in Table 1.

*PH due to lung diseases and/or hypoxia* One example of the third PH group is the high-altitude pulmonary edema (HAPE), a potentially lethal condition affecting previously healthy individuals rapidly going to high altitude [60]. The exact cause of HAPE remains unknown [31]. The favored hypothesis regarding its genesis is a severe and inhomogeneous vasoconstriction of the vasculature associated with a stress failure and an increase in transmural pressure  $P_C$  of the capillaries [60]. Rupture of the capillary wall causes fluid to flow from the capillary lumen to the interstitial and alveolar spaces. In order to simulate HAPE in our model, we start by randomly designating small regions of the lungs as edemic while the others remain unaffected, thus mimicking the typically patchy distribution of high-altitude-induced edemas [60]. Vasoconstriction is induced in the non-edemic regions only [60], thus increasing  $R_t$  and decreasing  $C_t$  via (5). In the edemic regions, the presence of fluid in the alveolar space causes the electrical conductivity of the parenchyma to increase. We consider an increase in

lung water concentration by 75 % [51]. In the model proposed by Roth et al. [47] for estimating the conductivity of lung parenchyma (Sect. 2.1.4), this corresponds to using an alveolar tissue conductivity  $\sigma_{alv} = 0.15$  S/m.

In a study on control and HAPE-susceptible subjects at high altitude, Maggiorini et al. [31] concluded that HAPE is initially caused by an increase in  $P_C$ . Although the exact quantitative relationship between  $P_A$  and  $P_C$  in HAPE is unknown, it stems from their study that  $P_A \approx 2 \cdot P_C$ . The remaining hemodynamic variables of the model, namely  $P_W$  and  $CI$ , remain normal in case of HAPE [60]. Maggiorini et al. reported values of  $P_W = 10.0$  mmHg and  $CI = 3.7$  L/min/m<sup>2</sup> for both control and HAPE-susceptible subjects at high altitude [31]. In our model, the abnormal increase in  $P_C$  can be simulated simply by setting  $P_W = P_C$ . Indeed, increasing  $P_W$  in the model can simulate either an increase in left atrial pressure (as is the case in PH-LHD) or an increase in transvenous pressure gradient (as is the case in HAPE).

The complete list of thus obtained hemodynamic parameter values to simulate each level of HAPE is provided in Table 1.

*Chronic thromboembolic pulmonary hypertension (CTEPH)* In the fourth group of PH, the disease is characterized by the partial or complete obliteration of one or several pulmonary arterial segments [42]. As a consequence, a part or the entirety of the flow is redirected toward the non-occluded areas, thereby exposing them to higher wall shear stresses [19]. An arteriopathy similar to that encountered in PAH (vasoconstriction and vascular remodeling) progressively develops in these segments, while the arteries downstream of the occluded areas typically remain unaffected [19, 42].

In the model, we simulate CTEPH by occluding one of the daughter vessels of the left interlobar artery and by inducing vasoconstriction in those parts of the microvasculature that are not downstream of the occluded segment. Pepke-Zaba et al. [42] reported average hemodynamic parameters in CTEPH from an international registry:  $P_A = 47.0$  mmHg and  $CI = 2.2$  L/min/m<sup>2</sup>. Left atrial pressure remains unaffected in CTEPH; Nagaya et al. reported a value of 8.0 mmHg for  $P_W$  [36]. Following the same procedure as the one used for PAH, we then find  $R_t$ ,  $C_t$  and  $CI$  for all levels of PAP.

The complete list of thus obtained hemodynamic parameter values to simulate each level of CTEPH is provided in Table 1.

### 2.3 EIT simulations and PTT estimation

With the ability to simulate various PAP-affecting pathologies in our 4D bio-impedance model, we can now proceed



to simulating EIT measurements for each of these pathologies using the model. All EIT simulations were performed with the EIDORS toolbox [2].

### 2.3.1 EIT simulations

*Obtaining surface voltage measurements (the forward problem)* The cardiac cycle, of duration  $T = 0.75$  s, was discretized into 25 time instants of 30 ms each, thus corresponding to an EIT image sampling rate of 33 frames/s. At each  $k$ -th time instant of the cardiac cycle, the first-order forward solver of EIDORS was used to simulate the propagation of small alternating electrical currents in the bioimpedance model (via the electrode belt shown in Fig. 2) and measure the resulting voltages  $\mathbf{v}_k$ . A voltage matrix  $\mathbf{V}$  was then obtained by concatenating horizontally all 25 column vectors  $\mathbf{v}_k$ .

Real EIT measurements are well known to include noise. In order to model noisy voltages, a realistic signal-to-noise ratio (SNR) was considered. In [50], the authors analyzed recordings from a Goe MF II EIT device (CareFusion, Germany) and found SNRs ranging from 42 to 156 dB. We chose a worst-case scenario SNR of 42 dB (i.e.,  $\text{SNR} = 15,850$ ). Following their approach, noisy voltages  $\mathbf{V}_n$  were thus obtained by adding a white Gaussian noise of variance  $\mathcal{P}_i/\text{SNR}$  to each  $i$ -th line of  $\mathbf{V}$ , where  $\mathcal{P}_i$  is the average power of the  $i$ -th line [50].

So-called difference voltages  $\mathbf{U}_n$  were then obtained by subtracting the first column (first frame) of  $\mathbf{V}_n$ , i.e., the end-diastolic voltages, from all columns (all frames) of  $\mathbf{V}_n$ , as is usual in medical EIT applications [20].  $\mathbf{U}_n$  thus describes voltage variations around a reference state (end diastole) and allows the linearization of the EIT reconstruction problem for small voltage variations around this working point.

*Reconstructing the internal conductivity distribution (the inverse problem)* Image reconstruction was carried out on a coarser version of the thoracic mesh using the widely used one-step Gauss–Newton algorithm with the Laplace prior [30]. Difference noisy EIT images  $\mathbf{Y}_n$  representing the intrathoracic conductivity changes over time with respect to the end-diastolic reference state were thus obtained as:

$$\mathbf{Y}_n = \mathbf{R}\mathbf{U}_n, \tag{9}$$

where  $\mathbf{R}$  is the so-called reconstruction matrix. Figure 7 shows an example of an EIT frame at end systole.

### 2.3.2 Pulmonary PTT estimation approach

In the following, the automatic procedure for estimating a pulmonary PTT value from a 25-frame EIT image sequence  $\mathbf{Y}_n$  is described.

First, a pulmonary region of interest (ROI), defined as those pixels depicting a lung-like behavior and a significant

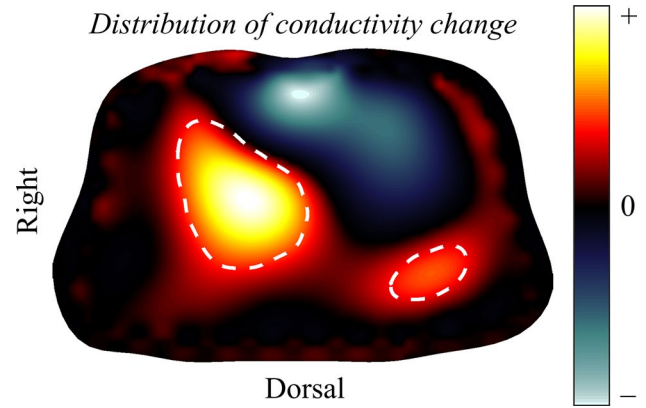


**Fig. 7** Example of reconstructed EIT frame (slice at the level of the EIT electrodes shown in Fig. 2) depicting the end-systolic distribution of conductivity change (with respect to end diastole). *Cool colors* (heart region) depict conductivity decreases with respect to end diastole, while *warm colors* (lung regions) depict conductivity increases. The pulmonary region of interest is highlighted by *dashed lines*. EIT tomographs provide functional information; they are known for not being anatomically accurate references. A lack of symmetry between the left and right lungs—as is the case here—is not unusual

pulsatility, was automatically segmented from the EIT images. To do so, the cardiac frequency Fourier coefficient  $z_T$  of the EIT time signal  $s(t)$  at each pixel was computed as:

$$z_T = \frac{1}{T} \int_0^T s(t)e^{-i\frac{2\pi t}{T}} dt. \tag{10}$$

At any given pixel location, the modulus  $|z_T|$  depicts the amplitude of the first cardiac harmonic whereas the argument  $\arg(z_T)$  depicts its phase shift with respect to the opening time of the pulmonary valve ( $t = 0$ ). As the conductivity increases in the lungs and decreases in the heart shortly after cardiac ejection, the first harmonic of  $s(t)$  resembles a sine wave ( $\pi/2$  phase shift) in the lungs whereas it resembles an antiphase sine wave ( $-\pi/2$  phase shift) in the heart. Both types of pixels were therefore separated by using a threshold value of 0 on  $\arg(z_T)$ . Pixels with significant pulsatility were then identified by comparing  $|z_T|$  to an automatic amplitude threshold  $\beta$  obtained using Otsu’s method [41]. Finally, the pulmonary ROI was obtained as those pixels for which  $|z_T| > \beta$  and  $\arg(z_T) > 0$  (Fig. 7).

For each pixel belonging to the pulmonary ROI, a PTT was estimated from its EIT time signal  $s(t)$  using the intersecting tangent method [8], resulting in  $M$  estimates of the pulmonary PTT for  $M$  pixels in the ROI. Erroneous PTT estimates were expected to arise in case of excessive noise or significant influence from sources not related to pulmonary pulsatility in  $s(t)$ , particularly in ROI pixels located near the cardiac region. In order to mitigate for these possible erroneous PTT estimates, outliers were automatically rejected using the median absolute deviation method [29].

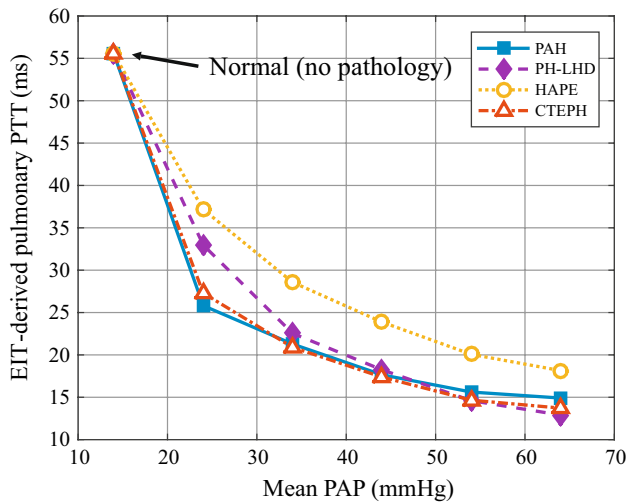


**Fig. 8** EIT-derived pulmonary PTT for different levels of PAP and for different pathologies

Finally, a representative pulmonary PTT value was obtained by averaging all non-rejected PTT estimates.

This whole process was carried out for all 21 vascular states summarized in Table 1. For each of them, the pulmonary PTT value estimated from the EIT images was then compared with the underlying PAP.

### 3 Results

Figure 8 shows the main findings of our study: For each type of hypertensive condition considered (PAH, PH-LHD, HAPE, CTEPH), the relation between the mean PAP and the PTT derived by EIT is shown. In the estimation of the PTT, an average of  $6.9 \pm 2.6$  % of pixels of the pulmonary ROI was rejected by the median absolute deviation method.

The next figures aim at illustrating the inner workings of our model and approach. Figure 9 illustrates the morphological differences that can be observed between the pressure waveforms traveling in the pulmonary arterial tree and the resulting EIT signals. The continuous lines depict an example of the pressure waveforms found at various arterial sites, from the main pulmonary artery to a pre-capillary artery, whereas the dotted line depicts the average EIT signal in the pulmonary ROI.

Figure 10 (top panel) depicts an example of the pressure waveforms as found in a distal artery for increasing levels of PAP. For each of them, their PTT value is highlighted with a marker. Similarly, the bottom panel depicts the corresponding average EIT signal in the pulmonary ROI, with their respective PTT values also highlighted. Comparing the PTT values calculated from the pressure waveforms with those calculated from the EIT signals, correlation

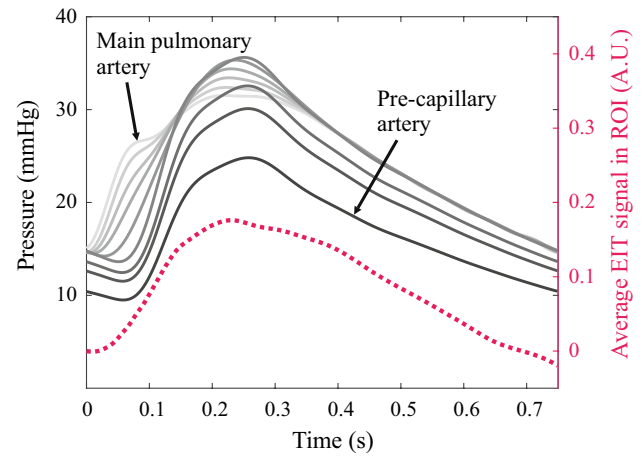


**Fig. 9** Continuous lines Pressure wave propagating through the pulmonary arterial tree in a borderline pre-hypertensive case of CTEPH. Dotted line Average EIT signal obtained in the pulmonary ROI in the same pathological condition

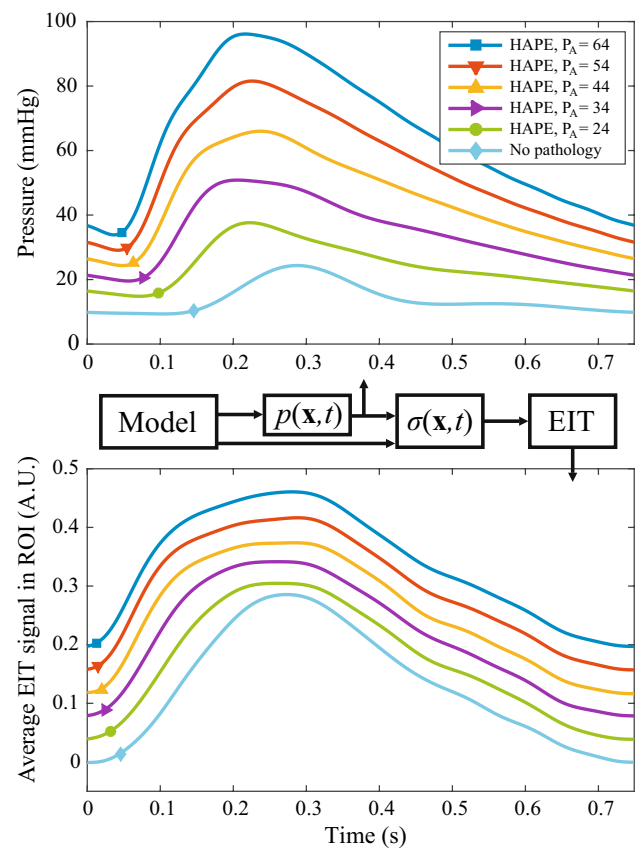


**Fig. 10** Top panel Example of pressure waveforms found in a distal artery for increasing levels of HAPE, as well as for the non-pathological case. Bottom panel Corresponding average EIT signals in the pulmonary ROI. In both panels, the PTT of each waveform is highlighted by a marker. Note that the EIT signals have been given arbitrary vertical offsets for easier visualization

coefficients  $r > 0.99$  ( $p < 0.001$ ) were found for all pathologies (PAH, PH-LHD, HAPE and CTEPH).

## 4 Discussion

In this study, we have hypothesized that changes in PAP could be monitored noninvasively by tracking changes in pulmonary PTT via EIT. To test our approach, we have used a realistic MRI-based 4D bio-impedance model of the human thorax. An anatomical model of the entire pulmonary arterial tree was constructed using contrast-enhanced magnetic resonance angiography scans [45] and a validated tree growing procedure [7]. The pulsatile behavior of each arterial segment of the tree was assessed via validated hemodynamic models of the pulmonary circulation [40, 45]. The local conductivity change occurring in each pulmonary voxel over time was obtained from the pressure-induced change in pulmonary blood volume. Several PAP-affecting pathologies were investigated. Simulated EIT measurements were performed on the model, and the pulmonary PTT was estimated from the resulting EIT signals.

### 4.1 EIT-based PAP monitoring

Figure 8 shows the main findings of the present study: It can be observed that increasing levels of PAP are associated with shorter PTT values for all forms of PH pathologies, as expected from the PWV principle (higher pressures are associated with faster PWV). These results suggest that EIT can be used to monitor changes in pulmonary PTT, and therefore in PAP. If confirmed experimentally, these results could be the opening wedge for noninvasive alternative solutions to the pulmonary artery catheter for patients with PH.

#### 4.1.1 On the pressure and EIT waveforms

Several other observations, listed hereafter, can be drawn from the figures presented in Sect. 3. Although the morphology of the EIT signal roughly resembles that of the various pressure waveforms (Fig. 9), it does not resemble one of them predominantly. In particular, the slope of the EIT signal is less steep than that of the pressure waveforms, which suggests that arteries of all sizes contribute to the generation of the EIT signal. The contribution of the small arteries is not negligible in comparison with that of the larger arteries as they are much more abundant [21].

Figure 10 shows how the PTT-related information carried by the pressure waveforms remains present in the EIT signals despite the aforementioned morphological differences between both types of waveforms. Note that all EIT signals depicted in Fig. 10 (bottom panel) have similar

peak-to-peak amplitudes, despite having been generated by vastly different distending pressures (top panel). This can be explained by the inverse exponential relationship between pressure ( $p$ ) and arterial distensibility ( $\delta$ ) [62]. As PAP rises to increasingly severe levels, arterial distensibility decreases due to vascular remodeling. As a consequence, the product of  $p$  and  $\delta$ , which determines the extent of arterial distension, remains almost constant throughout the physiological range of pressure values [28, 48]. Nevertheless, an amplitude decrease in the average EIT signal can be expected with an increase in PAP in cases of reduced pulmonary microvascular bed in advanced stages of PH [53].

#### 4.1.2 On the PTT–PAP relation

It can be observed from Fig. 8 that the PTT value at a given PAP level (e.g.,  $P_A = 24$  mmHg) is not necessarily the same for all pathologies. This is due to the physiological link between PWV and the structural properties of the arterial wall [62], which can strongly differ between pathologies. Conversely, in CTEPH, the arteriopathy in the non-occluded areas strongly resembles that of PAH [42], which explains why the PAP–PTT relation is very similar for both pathologies.

Finally, the inverse exponential nature of the PAP–PTT relation (Fig. 8) shows that the approach is best suited for tracking PAP changes in early stages of PH, as small changes in PAP induce large changes in PTT. The same observation was drawn in MRI studies [28, 48], where it was found that the distensibility of the main pulmonary artery started reaching a plateau level at around  $P_A > 40$  mmHg. Beyond this value, the arteries approach their elastic limit and the PWV does not increase significantly anymore [48].

### 4.2 Model assumptions validity, limitations and future work

We discuss hereafter the validity of the main assumptions used in the creation of our model, as well as its main limitations and those of our approach. We then mention practical workarounds to overcome some of these limitations and some suggested future work.

#### 4.2.1 Model assumptions validity

As mentioned in Sect. 2.1.1, our 4D bio-impedance model does not take into account impedance changes induced by respiratory activity. Respiration does not only affect the dielectric properties of the lung parenchyma, it also deforms the internal distribution of impedance volumes as well as the external thoracic contour. However, we consider

this simplification in our model to be acceptable, since several techniques (short apneas, electrocardiogram gating, frequency filtering, etc.) allow efficiently minimizing the influence of these respiratory artifacts in practice in cardiac EIT [11, 20]. Moreover, the automatic tracking of the pulmonary ROI (Sect. 2.3.2) can cope for possible respiration-induced changes in internal impedance distribution.

A second assumption of our model, mentioned in Sect. 2.1.3, is that the pressure downstream of our pulmonary arterial tree, i.e.,  $P_W$ , is continuous, although it is known to be slightly pulsatile [37]. In this study, we have considered the influence of the pulsatile component of  $P_W$  to be minor not only in terms of amplitude, but also because it occurs late in the cardiac cycle: The early systolic part of the  $\sigma(\mathbf{x}, t)$  waveform (Fig. 1), which is of interest to estimate the PTT, is not affected by the pulsatility of  $P_W$ . For this reason, its pulsatile component can, in our opinion, be neglected without any loss of relevant information.

A third assumption of our model is that the pulmonary arterial wall, known to be much thinner than its systemic counterpart [37], is of negligible thickness. The non-inclusion of the arterial wall in the model is expected to only slightly affect the baseline value of lung conductivity, but not its pulsatile behavior. The arteries will distend “at the same time” regardless of the presence (or absence) of the wall in the model. Thus, only the amplitude of the EIT signal  $s(t)$  is affected; its timing information (its PTT), which is of interest for PAP monitoring, remains unaffected.

#### 4.2.2 Model and approach limitations

A first limitation of our approach concerns the timing reference used for the estimation of the PTT. In our study,  $t = 0$  corresponds to the time of opening of the pulmonary valve. However, in practice, this feature is difficult to estimate noninvasively [35].

A second limitation concerns the possible influence of conductivity changes not related to pulmonary pulsatility in those lung regions close to the heart, in particular sources generating conductivity changes similar to those occurring in the lungs, such as atrial or aortic changes. Heart motion-induced displacements of the pulmonary arteries may also affect the pulmonary EIT signal in the most proximal regions of the lungs [43].

A third limitation, intrinsic to models describing complex processes, is the use of physiological parameters from multiple different studies, and therefore different sources.

#### 4.2.3 Practical workarounds

It is important to mention that workarounds exist in practice to try and overcome some of these limitations. For instance, PTT-based systemic blood pressure monitoring

systems often use the R-wave peak of the electrocardiogram—a robust feature to detect—as surrogate timing reference ( $t = 0$ ) for PTT estimation [35].

Erroneous PTT estimates resulting from the possible artifacts induced in the proximal regions of the lungs by sources not related to pulmonary pulsatility are expected to be automatically discarded by the outlier rejection method (Sect. 2.3.2) [29]. Alternatively, they could be avoided by limiting the ROI to its most distal part.

#### 4.2.4 Future work

Further improvement to the present model could aim at addressing the aforementioned limitations. However, in our opinion, future work should predominantly focus on evaluating our proposed noninvasive PAP monitoring approach in real EIT data.

## 5 Conclusions

There is currently no practical solution for the noninvasive monitoring of PAP in patients with PH. We have previously demonstrated experimentally the feasibility of a novel approach based on the use of EIT for the monitoring of systemic blood pressure [55]. In the present study, we evaluated its feasibility in the pulmonary circulation for the monitoring of PAP. Our results, obtained from simulations on a 4D bio-impedance model of the human thorax, suggest that changes in PAP can indeed be monitored by EIT under various pathophysiological conditions. If confirmed in clinical data, these findings could open the way for a novel generation of noninvasive PAP monitoring solutions for patients with PH.

**Acknowledgments** The authors would like to thank Dr. P. Reymond and T. Billiet (Ecole Polytechnique Fédérale de Lausanne, Switzerland) for providing the anatomical and circulatory models of the large pulmonary arteries, as well as Prof. A. Adler (Carleton University, Canada) for many valuable discussions. This work was supported in part by the Swiss National Science Foundation (SNSF) under Grant 205321-153364/1 and the SNSF/Nano-Tera project ObeSense (20NA21-1430801).

## References

1. Abraham WT, Adamson PB, Bourge RC et al (2011) Wireless pulmonary artery haemodynamic monitoring in chronic heart failure: a randomised controlled trial. *Lancet* 377:658–666
2. Adler A, Lionheart WRB (2006) Uses and abuses of EIDORS: an extensible software base for EIT. *Physiol Meas* 27:S25–S42
3. Afshar M, Collado F, Doukky R (2012) Pulmonary hypertension in elderly patients with diastolic dysfunction and preserved ejection fraction. *Open Cardiovasc Med J* 6:1–8
4. Billiet T (2009) Computational modeling of the hemodynamics in the pulmonary arterial tree: application to the human. M.S. thesis, Fac Eng Arch, Ghent Univ, Belgium

5. Borges JB, Suarez-Sipmann F, Bohm SH et al (2012) Regional lung perfusion estimated by electrical impedance tomography in a piglet model of lung collapse. *J Appl Physiol* 112:225–236
6. Braun F, Proença M, Rapin M et al (2015) 4D Heart Model Helps Unveiling Contributors to Cardiac EIT Signal. In: Proc EIT, Neuchâtel, Switzerland
7. Burrowes KS, Hunter PJ, Tawhai MH (2005) Anatomically based finite element models of the human pulmonary arterial and venous trees including supernumerary vessels. *J Appl Physiol* 99:731–738
8. Chiu YC, Arand PW, Shroff SG, Feldman T, Carroll JD (1991) Determination of pulse wave velocities with computerized algorithms. *Am Heart J* 121:1460–1470
9. Cox RH (1968) Wave propagation through a Newtonian fluid contained within a thick-walled, viscoelastic tube. *Biophys J* 8:691–709
10. Du Bois D, Du Bois EF (1989) A formula to estimate the approximate surface area if height and weight be known. 1916. *Nutrition* 5:303–311
11. Frerichs I, Pulletz S, Elke G, Reifferscheid F, Schädler D, Scholz J, Weiler N (2009) Assessment of changes in distribution of lung perfusion by electrical impedance tomography. *Respiration* 77:282–291
12. Galiè N, Humbert M, Vachiery JL et al (2016) 2015 ESC/ERS Guidelines for the diagnosis and treatment of pulmonary hypertension. *Eur Heart J* 37:67–119
13. Gille J, Seyfarth HJ, Gerlach S, Malcharek M, Czeslick E, Sablotzki A (2012) Perioperative anesthesiological management of patients with pulmonary hypertension. *Anesthesiol Res Pract* 2012:356982
14. Guazzi M, Borlaug BA (2012) Pulmonary hypertension due to left heart disease. *Circulation* 126:975–990
15. Guyton AC, Hall JE (2010) Pulmonary Circulation, Pulmonary Edema, Pleural Fluid. *Textbook of Medical Physiology*. W.B. Saunders Company, Philadelphia, pp 444–451
16. Harvey S, Harrison DA, Singer M et al (2005) Assessment of the clinical effectiveness of pulmonary artery catheters in management of patients in intensive care (PAC-Man): a randomised controlled trial. *Lancet* 366:472–477
17. Hasgall PA, Di Gennaro F, Baumgartner C, Neufeld E, Gosselin MC, Payne D, Klingeböck A, Kuster N (2015) IT'IS Database for thermal and electromagnetic parameters of biological tissues. Version 3.0, September 2015. Available: [www.itis.ethz.ch/database](http://www.itis.ethz.ch/database)
18. Hellige G, Hahn G (2011) Cardiac-related impedance changes obtained by electrical impedance tomography: an acceptable parameter for assessment of pulmonary perfusion? *Crit Care* 15:430
19. Hoepfer MM, Borlaug BA (2006) Chronic thromboembolic pulmonary hypertension. *Circulation* 113:2011–2020
20. Holder DS (ed) (2005) Electrical impedance tomography: methods, history and applications. Institute of Physics Publishing, Bristol
21. Huang W, Yen RT, McLaurine M, Bledsoe G (1996) Morphometry of the human pulmonary vasculature. *J Appl Physiol* 81:2123–2133
22. Humbert M, Sitbon O, Chaouat A et al (2006) Pulmonary arterial hypertension in France: results from a national registry. *Am J Resp Crit Care* 173:1023–1030
23. Kitabatake A, Inoue M, Asao M et al (1983) Noninvasive evaluation of pulmonary hypertension by a pulsed Doppler technique. *Circulation* 68:302–309
24. Koledintseva MY, DuBroff RE, Schwartz RW (2006) A Maxwell Garnett Model for Dielectric Mixtures Containing Conducting Particles at Optical Frequencies. *Prog Electromagn Res* 63:223–242
25. Kovacs G, Berghold A, Scheidl S, Olschewski H (2009) Pulmonary arterial pressure during rest and exercise in healthy subjects: a systematic review. *Eur Respir J* 34:888–894
26. Lankhaar JW, Westerhof N, Faes TJC, Marques KJM, Marcus JT, Postmus PE, Vonk-Noordegraaf A (2006) Quantification of right ventricular afterload in patients with and without pulmonary hypertension. *Am J Physiol-Heart C* 291:H1731–H1737
27. Lankhaar JW, Westerhof N, Faes TJC et al (2008) Pulmonary vascular resistance and compliance stay inversely related during treatment of pulmonary hypertension. *Eur Heart J* 29:1688–1695
28. Lau EM, Iyer N, Ihsar R, Bailey BP, Adams MR, Celermajer DS (2012) Abnormal pulmonary artery stiffness in pulmonary arterial hypertension: in vivo study with intravascular ultrasound. *PLoS One* 7:e33331
29. Leys C, Ley C, Klein O, Bernard P, Licata L (2013) Detecting outliers: do not use standard deviation around the mean, use absolute deviation around the median. *J Exp Soc Psychol* 49:764–766
30. Lionheart WRB (2004) EIT reconstruction algorithms: pitfalls, challenges and recent developments. *Physiol Meas* 25:125–142
31. Maggiorini M, Mélot C, Pierre S et al (2001) High-altitude pulmonary edema is initially caused by an increase in capillary pressure. *Circulation* 103:2078–2083
32. Mathew JP, Newman MF (2001) Hemodynamic and Related Monitoring. In: Estafanous FG, Barash PG, Reves JG (eds) *Cardiac Anesthesia: Principles and Clinical Practice*, 2nd edn. Lippincott Williams & Wilkins, Philadelphia, pp 195–236
33. McGoon MD, Kane GC (2009) Pulmonary hypertension: diagnosis and management. *Mayo Clin Proc* 84:191–207
34. Milnor WR (1989) *Hemodynamics*, 2nd edn. Lippincott Williams & Wilkins, Baltimore
35. Mukkamala R, Hahn JO, Inan OT, Mestha LK, Kim CS, Töreyn H, Kyal S (2015) Towards ubiquitous blood pressure monitoring via pulse transit time: Theory and practice. *IEEE T Bio-Med Eng* 62:1879–1901
36. Nagaya N, Ando M, Oya H, Ohkita Y, Kyotani S, Sakamaki F, Nakanishi N (2002) Plasma brain natriuretic peptide as a non-invasive marker for efficacy of pulmonary thromboendarterectomy. *Ann Thorac Surg* 74:180–184
37. Nichols W, O'Rourke M (2005) *The pulmonary circulation. McDonald's blood flow in arteries: theoretical, experimental and clinical principles*, 5th edn. Hodder Arnold, London, pp 307–320
38. Nopp P, Rapp E, Pfützner H, Nakesch H, Ruhsam C (1993) Dielectric properties of lung tissue as a function of air content. *Phys Med Biol* 38:699–716
39. Olufsen MS (1998) Modeling the Arterial System with Reference to an Anesthesia Simulator. Ph.D. dissertation no. 345, IMFUFA, Rostkilde Univ, Denmark
40. Olufsen MS (2004) Modeling Flow and Pressure in the Systemic Arteries. *Applied Mathematical Models in Human Physiology*. SIAM, Philadelphia, pp 91–136
41. Otsu N (1979) A threshold selection method from gray-level histograms. *IEEE Trans Syst Man Cybern* 9:62–66
42. Pepke-Zaba J, Delcroix M, Lang I et al (2011) Chronic thromboembolic pulmonary hypertension (CTEPH): results from an international prospective registry. *Circulation* 124:1973–1981
43. Proença M, Braun F, Rapin M et al (2015) Influence of heart motion on cardiac output estimation by means of electrical impedance tomography: a case study. *Physiol Meas* 36:1075–1091
44. Qureshi MU, Vaughan GDA, Sainsbury C, Johnson M, Peskin CS, Olufsen MS, Hill NA (2014) Numerical simulation of blood flow and pressure drop in the pulmonary arterial and venous circulation. *Biomed Model Mechn* 13:1137–1154
45. Reymond P (2011) Pressure and flow wave propagation in patient-specific models of the arterial tree. Ph.D. dissertation no. 5029, LHTC, EPFL, Lausanne, Switzerland

46. Rich S, D'Alonzo GE, Dantzker DR, Levy PS (1985) Magnitude and implications of spontaneous hemodynamic variability in primary pulmonary hypertension. *Am J Cardiol* 55:159–163
47. Roth C, Ehrl A, Becher T, Frerichs I, Schittny JC, Weiler N, Wall WA (2015) Correlation between alveolar ventilation and electrical properties of lung parenchyma. *Physiol Meas* 36:1211–1226
48. Sanz J, Kariisa M, Dellegrottaglie S, Prat-González S, Garcia MJ, Fuster V, Rajagopalan S (2009) Evaluation of pulmonary artery stiffness in pulmonary hypertension with cardiac magnetic resonance. *JACC Cardiovasc Imaging* 2:286–295
49. Saouti N, Westerhof N, Postmus PE, Vonk-Noordegraaf A (2010) The arterial load in pulmonary hypertension. *Eur Respir Rev* 19:197–203
50. Schlebusch T, Nienke S, Leonhardt S, Walter M (2014) Bladder volume estimation from electrical impedance tomography. *Physiol Meas* 35:1813–1823
51. Schuster DP, Anderson C, Kozlowski J, Lange N (2002) Regional pulmonary perfusion in patients with acute pulmonary edema. *J Nucl Med* 43:863–870
52. Shi Y, Lawford P, Hose R (2011) Review of zero-D and 1-D models of blood flow in the cardiovascular system. *Biomed Eng Online* 10:1–38
53. Smit HJ, Vonk-Noordegraaf A, Boonstra A, de Vries PM, Postmus PE (2006) Assessment of the pulmonary volume pulse in idiopathic pulmonary arterial hypertension by means of electrical impedance tomography. *Respiration* 73:597–602
54. Solà J, Rimoldi SF, Allemann Y (2010) Ambulatory monitoring of the cardiovascular system: the role of pulse wave velocity. *New Developments in Biomedical Engineering*. InTech, Rijeka, pp 391–424
55. Solà J, Adler A, Santos A, Tusman G, Suarez-Sipmann F, Bohm SH (2011) Non-invasive monitoring of central blood pressure by electrical impedance tomography: first experimental evidence. *Med Biol Eng Comput* 49:409–415
56. Solà J, Ferrario D, Adler A, Proença M, Brunner JX (2013) Method and apparatus for the non-invasive measurement of pulse transit times (PTT) (2013, Dec. 4). Patent EP 2593006 B1. Available: <http://www.google.com/patents/EP2593006B1>
57. Strange G, Playford D, Stewart S, Deague JA, Nelson H, Kent A, Gabbay E (2012) Pulmonary hypertension: prevalence and mortality in the Armadale echocardiography cohort. *Heart* 98:1805–1811
58. Tedford RJ, Hassoun PM, Mathai SC et al (2012) Pulmonary Capillary Wedge Pressure Augments Right Ventricular Pulsatile Loading. *Circulation* 125:289–297
59. van de Vosse FN, Stergiopoulos N (2011) Pulse wave propagation in the arterial tree. *Annu Rev Fluid Mech* 43:467–499
60. West JB (2007) High altitude pulmonary edema. High altitude medicine and physiology, 2nd edn. Hodder Arnold, London, pp 279–298
61. Westerhof N, Lankhaar JW, Westerhof BE (2009) The arterial windkessel. *Med Biol Eng Comput* 47:131–141
62. Westerhof N, Stergiopoulos N, Noble MIM (2010) Snapshots of Hemodynamics: An Aid for Clinical Research and Graduate Education, 2nd edn. Springer Science & Business Media, New York
63. Wiener F, Morkin E, Skalak R, Fishman AP (1966) Wave propagation in the pulmonary circulation. *Circ Res* 19:834–850

**Martin Proença** He received his M.S. degree in Information Technology from the Swiss Federal Institute of Technology (EPFL), Lausanne, Switzerland, in 2011, after completing his master thesis within the biomedical R&D group at the Swiss Center for Electronics and Microtechnology (CSEM), Neuchâtel, Switzerland. He completed his academic studies with a Minor in Biomedical Technology in the field of biomedical image analysis and particle tracking. Since 2011, he is

working as an R&D engineer in the biomedical group of the Systems division at CSEM, where he is involved in several research and industrial projects in the domains of blood pressure, pulse oximetry, core body temperature and bio-impedance. He is currently doing his Ph.D. thesis within EPFL and CSEM in the field of hemodynamic parameters estimation via electrical impedance tomography.

**Fabian Braun** He received his B.Sc. in Electrical Engineering from the University of Applied Sciences Rapperswil (HSR), Switzerland, in 2010. During his time at HSR, he had the opportunity to join the Institute of Electrical Engineering and Computer Science at the University of Stavanger (UiS), Norway. After a short period in industry as embedded software engineer, he pursued his academic career at the Eidgenössische Technische Hochschule Zürich (ETHZ), Zürich, Switzerland, where he received his M.Sc. degree in Biomedical Engineering in 2013. During this period, he joined the Signal Processing group of the Swiss Center for Electronics and Microtechnology (CSEM), Neuchâtel, Switzerland, to complete his master thesis. He is currently doing his Ph.D. thesis within the Swiss Federal Institute of Technology (EPFL), Lausanne, Switzerland, and CSEM in the field of noninvasive cardiovascular monitoring using electrical impedance tomography. At CSEM, he is further involved in other research and industrial projects in the fields of pulse oximetry, EIT and others, generally involving the noninvasive assessment of physiological parameters.

**Josep Solà** He received his M.S. degree on Telecommunication Engineering from the Universitat Politècnica de Catalunya (UPC), Barcelona, Spain, after writing his master thesis within the R&D department of SONY International, Germany. In 2011, he received his Ph.D. from the Eidgenössische Technische Hochschule Zürich (ETHZ), Zürich, Switzerland, in the field of noninvasive blood pressure monitoring. He joined the biomedical team at the Swiss Center for Electronics and Microtechnology (CSEM), Neuchâtel, Switzerland, in 2004, where he is currently senior R&D engineer. His domains of expertise go from the development of high-level signal processing algorithms, to their embedded implementation in fixed-point microprocessors. Specialized on the monitoring of the human cardiovascular system, he is currently involved in research and industrial projects in the fields of blood pressure, cardiac output, pulse oximetry and energy expenditure.

**Jean-Philippe Thiran** He is an Associate Professor in Signal Processing at the Swiss Federal Institute of Technology (EPFL), Lausanne, Switzerland. He also holds a 20 % associate professor position with the Department of Radiology of the University Hospital Center and University of Lausanne (CHUV-UNIL). His current scientific interests include image analysis and computer vision, medical imaging and multimodal signal/image processing, with application to brain connectivity analysis, remote sensing, human–computer interactions, etc. Prof. Thiran is author or co-author of several book chapters, of 150 journal papers and of more than 200 conference papers in image processing and analysis. He holds seven international patents. From 2001 to 2005, he was Co-Editor-in-Chief of the Signal Processing international journal (published by Elsevier Science). Until 2015 he was an associate editor of the IEEE Transactions on Image Processing. Among other duties, he was the general chairman of the 2008 European Signal Processing Conference (EUSIPCO 2008) and the technical co-chair of the 2015 IEEE International Conference on Image Processing (ICIP 2015). He is a senior member of the IEEE.

**Mathieu Lemay** He received his B.Sc. degree in Electrical Engineering from the Université Laval, Quebec city, Canada, and his Ph.D. from the Swiss Federal Institute of Technology (EPFL), Lausanne, Switzerland, in 2003 and 2007, respectively. He joined the Signal Processing section of the Swiss Center for Electronics and Microtechnology (CSEM), Neuchâtel, Switzerland, during summer 2011

after 4 years of Postdoctoral positions at EPFL and at the Universität Bern, Bern, Switzerland. He currently involved in several research and development projects, mainly oriented in biomedical field (electrocardiogram, heart rate, activity classification) including European

projects (work package leader of the system design and embedded software for PEGASO). His current research interests include heart arrhythmias, mainly atrial fibrillation, therapies and related signal processing techniques.